Petroleum Science 23 (2026) 836–850

Contents lists available at ScienceDirect

Petroleum Science

journal homepage: www.keaipublishing.com/en/journals/petroleum-science

Original Paper

A novel approach to evaluating remaining oil potential using dynamic connectivity and bivariate mapping in large-scale reservoirs

Jun-Da Wu *, Tao Chang, Yi-Fan He, Quan-Lin Wang, Di Wang

Tianjin Branch, CNOOC China Limited, Tianjin, 300459, China

ARTICLE INFO

Article history:
Received 12 June 2024
Received in revised form
9 December 2025
Accepted 10 December 2025
Available online 16 December 2025

Edited by Yan-Hua Sun

Keywords:
Waterflooding
Remaining oil evaluation
Dynamic connectivity
Bivariate mapping
Numerical simulation

ABSTRACT

In the development of water flooding reservoirs, enhancing oil recovery often requires implementing measures tailored to the reservoir's specific characteristics. A critical step in this process is evaluating the remaining oil potential, which directly influences the effectiveness of recovery strategies. However, evaluating the remaining oil potential in large reservoirs is challenging due to reservoir heterogeneity and complex well patterns. Existing evaluation methods are often cumbersome and lack intuitiveness. To address these issues, this study proposes a novel method for evaluating remaining oil potential by utilizing reservoir dynamic connectivity and remaining oil abundance. This method draws upon the advantages of the Eikonal equation in accurately describing the pressure wavefront and its propagation speed. By replacing traditional analytical methods with bivariate mapping, this approach effectively visualizes and correlates dynamic and static attributes. On this basis, the reservoir is classified into four regions: uneconomic/awaiting measures, low-efficiency waterflooding, major potential, and primary production. The potential of each region is intuitively analyzed and evaluated, offering clear insights into development status, untapped potential, and optimal strategies for reservoirs within each region. The application of this method to the M oilfield in the Bohai Sea yielded promising results across three distinct scenarios aimed at enhancing recovery: horizontal well water control, injection–production system optimization, and infill horizontal well deployment. These successful outcomes highlight the applicability of this method to complex, large-scale reservoirs and highlight its potential as a valuable tool for guiding recovery strategies in other challenging reservoir environments.

1. Introduction

Prolonged development in water flooding reservoirs often exacerbates complexities such as reservoir heterogeneity, non-optimal well patterns, and inefficient injection strategies, resulting in uneven water distribution across the reservoir. This often leads to ineffective circulation of injected water in dominant zones, severely hindering the recovery of low-permeability and poorly controlled zones. To improve development efficiency and enhance economic effectiveness, it is essential to adjust injection strategies, flow fields, and well patterns to sustain oilfield production. However, due to significant variations in remaining oil abundance and reservoir connectivity across different regions, it is critical to select development measures or strategies tailored to these differences. To comprehensively and scientifically evaluate the remaining oil potential, it is essential to develop an assessment method that effectively captures both the degree of remaining oil enrichment and fluid flow capacity. Such an approach can more effectively guide the implementation of measures, thus enhancing oilfield development effectiveness.

In recent years, extensive research has been conducted on methods for evaluating the remaining oil potential, primarily including pattern recognition methods, numerical simulation methods, and artificial intelligence methods.

Pattern recognition methods primarily rely on key parameters from geological and geophysical data. They analyze macroscopic patterns in sedimentation (Dam et al., 2023; Zhu et al., 2021; Zubkov, 2017), tectonics (Lu et al., 2022; Zhao et al., 2020), flow units (Lopez Jimenez and Aguilera, 2015; Liu et al., 2022; Lu et al., 2020), and other aspects to qualitatively describe the enrichment

* Corresponding author.
E-mail address: wujd7@cnooc.com.cn (J.-D. Wu).
Peer review under the responsibility of China University of Petroleum (Beijing).

https://doi.org/10.1016/j.petsci.2025.12.018

patterns of oil at different locations within the reservoir. The method primarily adopts a geological and geophysical perspective, providing a broader-scale description, with inherent subjectivity and uncertainty (Alpak et al., 2010). It is commonly employed during the exploration phase or early stage of development when limited production data are available, posing challenges in guiding the detailed development of complex large-scale reservoirs in later stages.

Numerical simulation is a method for modeling the movement of underground fluids through mathematical equations. Based on history matching, it predicts the distribution pattern of remaining oil (Augustine et al., 2021; Hoffman and Reichhardt, 2020; Sikanyika et al., 2022; Wang et al., 2020) and reveals the flow field (Batycky and Thiele, 2016; Chen et al., 2020; Datta-Gupta and King, 2007; Zhang et al., 2021). This method is the most commonly used tool for potential analysis and evaluation during the late-stage development of large oilfields. However, the analysis of remaining oil potential often depends on static parameters, such as oil saturation, which fail to capture dynamic factors like reservoir connectivity. As a result, these parameters alone are frequently insufficient to accurately inform the implementation of effective development measures. In many cases, further data processing and analysis are still required for more in-depth investigation.

The artificial intelligence method is a newly emerging approach for evaluating the remaining oil potential in recent years. It is based on large volumes of production test data and utilizes various intelligent algorithms such as cluster analysis (Siena et al., 2016; Zhang et al., 2022), neural networks (Ramos and Akanji, 2017; Tabatabaei et al., 2023; Zhang et al., 2019), random forests (Mahdaviara et al., 2022; Zhang et al., 2019), to predict the remaining oil potential in different regions. The application of this method requires a substantial data sample, with variables such as the training process, sample quality, and model selection significantly influencing the accuracy of the assessment (Cheraghi et al., 2021). Although this method often demonstrates strong performance in theoretical models, its limitations in accuracy and applicability have impeded its widespread adoption in real-world oil fields.

Each of the methods discussed has its own limitations. While some studies have attempted to combine them, they still lack intuitive presentation and accurate guidance. To tackle these issues, this study proposes a new method for evaluating the remaining oil potential based on reservoir dynamic connectivity and remaining oil abundance. By considering both key dynamic and static parameters, a bivariate mapping approach is employed to construct a chart for tapping remaining oil potential. This approach facilitates a visual analysis and evaluation of reservoir remaining oil potential within a three-dimensional numerical simulation model.

2. Methodology

To more accurately evaluate the oil potential of different regions at various reservoir stages, this study conducts a secondary analysis of numerical simulation results, based on the evaluation of reservoir dynamic connectivity and remaining oil abundance. The specific workflow is illustrated in Fig. 1.

First, this study proposes a method for evaluating reservoir dynamic connectivity by taking advantage of the accuracy in using the Eikonal equation to describe the pressure wavefront. The fast marching method (FMM) is then utilized for numerical difference calculations to match the grid structure of numerical simulation. Using a single-layer reservoir model as an example, the method's applicability and accuracy were validated across various reservoir properties, well patterns, and development stages.

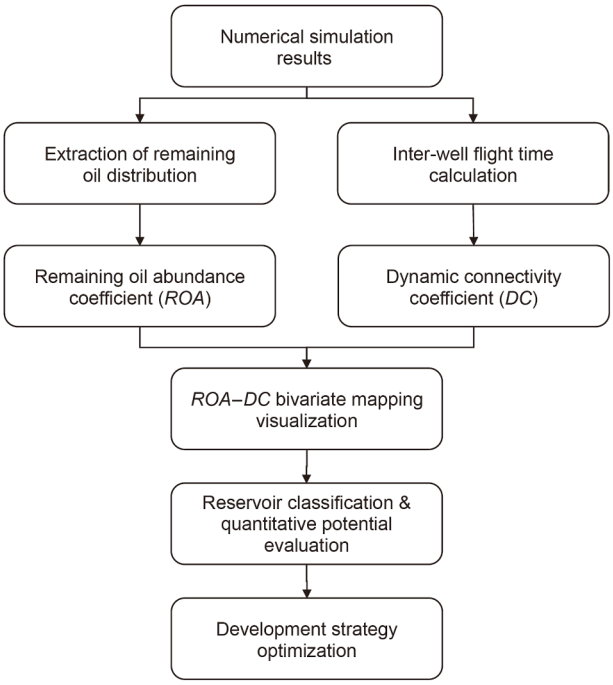

Fig. 1. The research workflow in this study.

Second, the remaining oil abundance coefficient (*ROA*) and the dynamic connectivity coefficient (*DC*) were calculated and integrated through bivariate mapping to establish a reservoir potential assessment chart. The potential analysis results of a three-dimensional reservoir under bivariate conditions are intuitively presented by depicting the differences and variations using color. Based on the bivariate mapping, the reservoir is divided into four regions: uneconomic/awaiting measure, low-efficiency waterflooding, major potential, and primary production. This classification clearly delineates the development potential of different regions and provides direction for subsequent exploration and development. The method was utilized to conduct a comprehensive simulation analysis on a multi-layer model of the 3D EGG reservoir. This demonstrates the method's precise evaluation capability for determining remaining oil potential at various stages of water flooding and its ability to guide potential tapping in different regions.

Finally, this method was applied to the high water-cut development stage of the M oilfield in the Bohai Sea, demonstrating its applicability in complex large reservoirs through three different examples of potential tapping: water control for horizontal well, injection–production system adjustment, and infill horizontal well.

3. Method for calculating dynamic connectivity of reservoirs

3.1. Description of pressure wave propagation based on the Eikonal equations

Descriptions of wave propagation have been extensively applied in various fields such as optics, engineering mechanics, and geophysics. In reservoir engineering, pressure propagation within porous media is analogous to wave propagation (Datta-Gupta et al., 2011), where production wells and injection wells

function as sources and sinks for pressure propagation. The instantaneous pressure response in heterogeneous reservoirs can be expressed as follows:

$$\varphi(x)c_t\frac{\partial P(x,t)}{\partial t}=\nabla\cdot\left(\frac{K(x)}{\mu}\nabla P(x,t)\right) \tag{1}$$

where φ is the rock porosity, dimensionless; K is the permeability, mD; μ is the fluid viscosity, Pa·s; c_t is the rock compressibility, Pa^{-1}; P is the pressure, Pa.

Eq. (2) is derived using the Fourier transform.

$$\varphi(x)c_t(-i\omega)\tilde{P}(x,\omega)=\frac{K(x)}{\mu}\nabla^2\tilde{P}(x,\omega)+\nabla\frac{K(x)}{\mu}\cdot\widetilde{\nabla P}(x,\omega) \tag{2}$$

where i is the imaginary unit, dimensionless; ω is the frequency in the Fourier transform, rad/s; $\tilde{P}$ is the pressure in the frequency domain, Pa.

Using the power term representation of the $\sqrt{-i\omega}$ reciprocal, the asymptotic solution to Eq. (2) is derived as follows:

$$\tilde{P}(x,\omega)=e^{-\sqrt{-i\omega}\tau(x)}\sum_{k=0}^{\infty}\frac{A_k(x)}{\left(\sqrt{-i\omega}\right)^k} \tag{3}$$

where A_k is the amplitude of the k-th-order pressure wave, Pa; τ is the propagation time of the pressure wave (also known as the flight time), $s^{0.5}$.

When $k=0$, the expression for the high-frequency solution is derived, which can also be understood physically as the propagation of the pressure wavefront in the reservoir (Vasco et al., 2000).

$$\tilde{P}(x,\omega)=A_0(x)e^{-\sqrt{-i\omega}\tau(x)} \tag{4}$$

By substituting Eq. (4) into Eq. (2), the governing equation for the propagation of the pressure wavefront in non-homogeneous porous media is derived as follows:

$$F(x)|\nabla\tau(x)|=1 \tag{5}$$

where $F(x)$ represents the interface velocity function, $m\cdot s^{-0.5}$. It is expressed as follows:

$$F(x)=\sqrt{\frac{K(x)}{\varphi(x)c_t}\left(\frac{K_{ro}(x)}{\mu_o}+\frac{K_{rw}(x)}{\mu_w}\right)} \tag{6}$$

3.2. Fast marching method

The fast marching method (FMM) is an efficient approach for solving the Eikonal equation on a finite difference grid (Sethian and Popovici, 1999). It replaces the differential operator with a specialized quotient to accurately track the wavefront of pressure propagation. The FMM algorithm is a single-pass method with low computational complexity and high efficiency, making it particularly well-suited for large-scale reservoir simulation. For an $N\times N$ grid model, the number of calculations is less than $N\log N$, which is significantly faster than traditional finite difference algorithms and 2 to 3 orders of magnitude faster than streamline simulation.

In three-dimensional case, the equations solved using the FMM are as follows:

$$\max\left(\frac{\tau-\tau_x}{\Delta x},0\right)^2+\max\left(\frac{\tau-\tau_y}{\Delta y},0\right)^2+\max\left(\frac{\tau-\tau_z}{\Delta z},0\right)^2=\frac{1}{F^2} \tag{7}$$

$$F=\sqrt{\frac{K(x)K_r(x)}{\mu c_t(x)\varphi(x)}} \tag{8}$$

$$\tau_x=\min\left(\tau_{i-1,j,k},\tau_{i+1,j,k}\right) \tag{9}$$

$$\tau_y=\min\left(\tau_{i,j-1,k},\tau_{i,j+1,k}\right) \tag{10}$$

$$\tau_z=\min\left(\tau_{i,j,k-1},\tau_{i,j,k+1}\right) \tag{11}$$

Taking Fig. 2 as an example, the main computational steps for solving the Eikonal equation using the FMM are outlined as follows:

(a) Define the initial grid and mark it as the frozen grid.
(b) Identify the adjacent grids of the frozen grid and calculate the flight time (τ) required for propagation from the frozen grid to these adjacent grids.
(c) Select the adjacent grid with the shortest flight time (τ) and mark it as the next frozen grid.
(d) Expand the set of frozen grids by including the newly frozen grid. For all grids currently in the frozen grid set, calculate the flight time (τ) to their adjacent grids, and update the set of frozen grids accordingly.
(e) Repeat steps (b) to (d) until all grids are marked as frozen.

Because FMM avoids finite difference calculations, it significantly reduces the computational time required by traditional numerical simulation methods. Therefore, it can be applied to grids containing tens of millions or even billions of cells. This capability makes it highly effective for the detailed characterization of reservoir dynamic connectivity in large-scale reservoirs.

3.3. Calculation of reservoir dynamic connectivity

For an actual reservoir, production wells and injection wells serve as source and sink terms, generating pressure disturbances that affect the fluid flow within the reservoir. In this study, the propagation time of the pressure wavefront from an injection well to the i-th grid is denoted as τ_{Ii}, while the propagation time from the i-th grid to a production well is denoted as τ_{iP}. The sum of these times is referred to the inter-well flight time τ_{IiP} at the i-th grid, as illustrated in Fig. 3.

Due to reservoir heterogeneity, flight times between wells vary significantly across different reservoir regions. Furthermore, as the reservoir development progresses, the fluid distribution within the reservoir and well pattern adjustments can directly influence inter-well flight times in various regions. Reservoir dynamic connectivity at different development stages can be assessed by the inter-well flight time, which represents the speed of pressure wavefront propagation.

3.4. Case 1: 2D mechanistic model

The precise characterization of pressure propagation using the Eikonal equation, coupled with the efficient computational approach of FMM has led to a high level of applicability in the reservoir dynamic connectivity.

The SPE10 model was chosen as the foundational dataset for this study. This dataset, widely utilized in numerical simulation research, is publicly available on the SPE website (http://www.spe.org/web/csp). To comprehensively evaluate the feasibility and

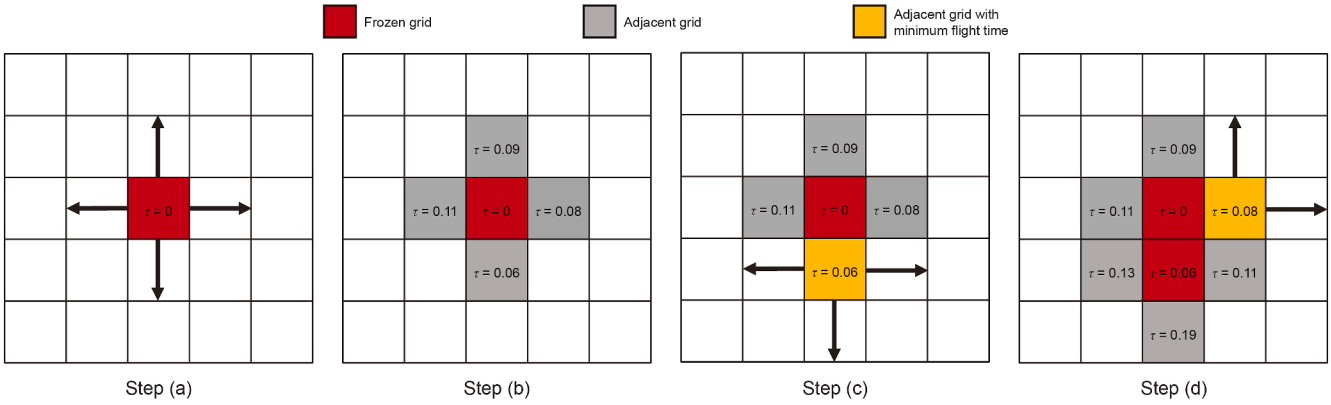

Fig. 2. Schematic of the FMM calculation process.

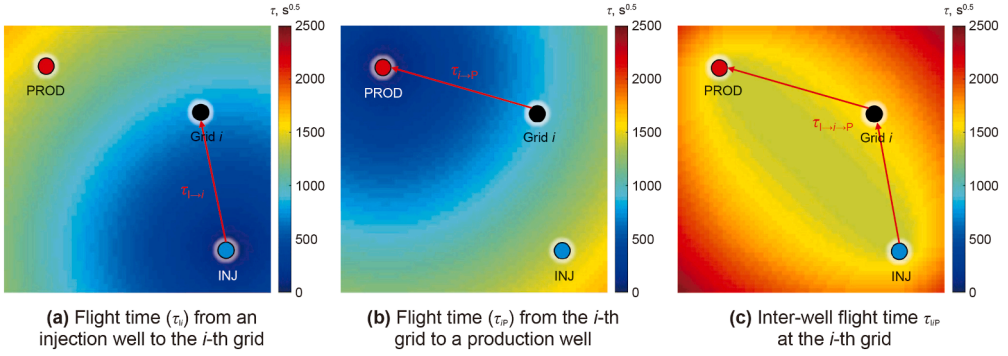

Fig. 3. Schematic of inter-well flight time calculation.

adaptability of the proposed method under various conditions, permeability data from the 21st layer of the SPE10 benchmark model were utilized. The original data was scaled and augmented with random noise to construct a 2D mechanistic model, with its permeability distribution and histogram depicted in Fig. 4. The permeability of the model ranged from 5 to 400 mD, with an average of 53 mD.

3.4.1. Heterogeneity consideration

In heterogeneous reservoirs, pressure wavefronts propagate preferentially through high-permeability regions due to the faster interface velocity (F). As shown in Fig. 5(b), variations in inter-well flight time are represented by different colors. The color gradient from red to yellow to blue corresponds to a reduction in inter-well flight time, indicating stronger connectivity in these regions. In

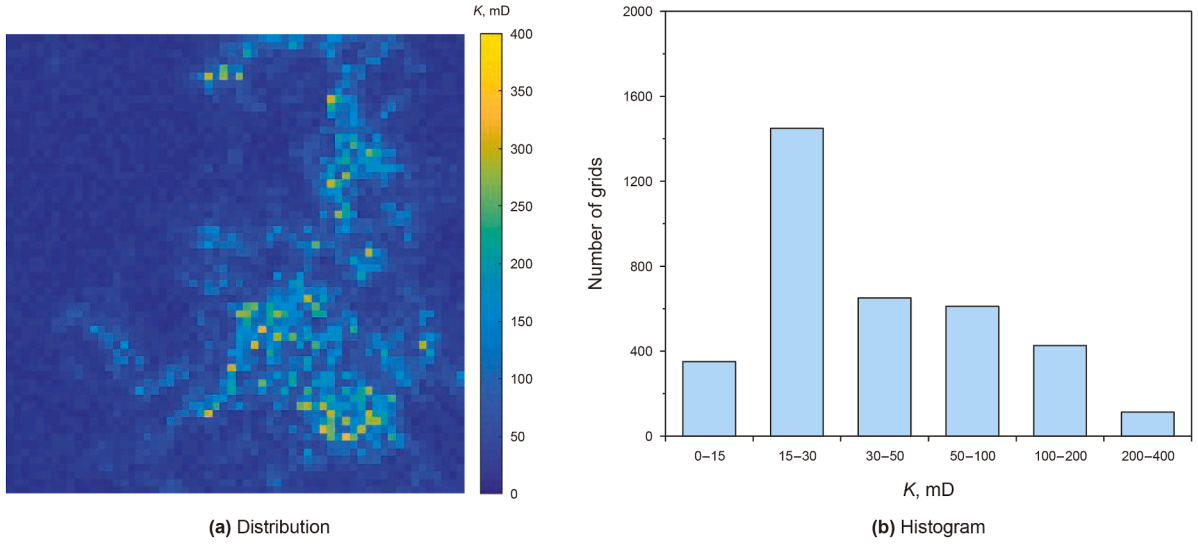

Fig. 4. Permeability distribution and histogram of reservoir model.

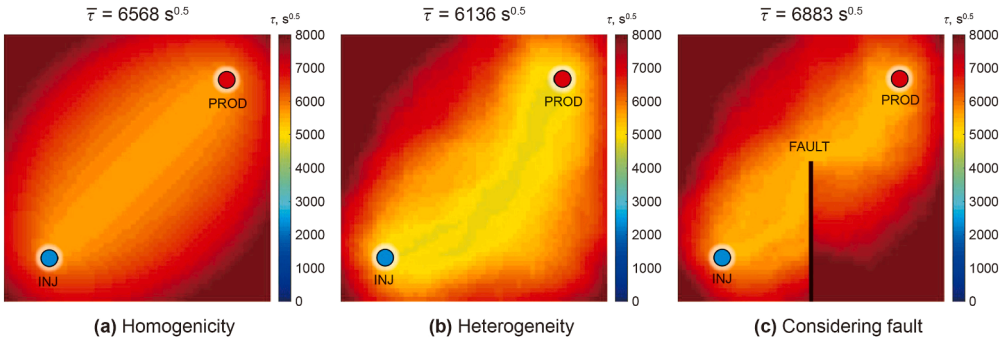

Fig. 5. Dynamic connectivity of reservoirs with different properties.

this heterogeneous model, the low-permeability region in the top-left corner is shown with a more reddish hue, indicating significantly poorer dynamic connectivity in that region. The higher average permeability of the heterogeneous model (53 mD), compared to the homogeneous model (35 mD), is associated with a reduction in the average inter-well flight time (from 6568 to 6136 $s^{0.5}$), reflecting an improvement in the overall connectivity of the reservoir.

3.4.2. Fault consideration

In real reservoir models, faults often need to be considered for their impact on connectivity. For 2D or 3D models, faults are modeled by assigning zero permeability to grid cells adjacent to the fault. This prevents pressure waves from penetrating the fault, thereby influencing flight time on both sides. A vertical fault was introduced below the reservoir in the mechanistic model, as shown in Fig. 5(c). The calculation results indicate that the fault blocks the propagation of the pressure wavefront, significantly increasing the inter-well flight time in the lower-right corner. This greatly affects the connectivity of reservoirs in this region and also alters the connectivity between injection and production wells, which aligns with conventional understanding. Additionally, the fault affects the overall connectivity of the reservoir, increasing the average inter-well flight time to 7000 $s^{0.5}$.

3.4.3. Well type consideration

Due to reservoir heterogeneity, horizontal wells are widely employed in the development of narrow and thin reservoirs, as well as in similar scenarios. For such wells, which simulate perforation operations in numerical models, the FMM represents them as a multi-source sink problem for computational purposes. The simulation results are shown in Fig. 6(a). Compared to vertical wells, horizontal wells have a broader area of influence, which significantly improves overall reservoir connectivity, reducing the average inter-well flight time from 6136 to 4594 $s^{0.5}$.

3.4.4. Well pattern consideration

In large reservoir numerical simulation, it is necessary to consider multi-source and sink problems caused by well interference due to the presence of numerous wells. The Eikonal equation is well-suited to simulate the propagation of the pressure wavefront under conditions of multi-well interference. Taking the example of a five-spot well pattern (Fig. 6(b)), the increased number of wells and the greater degree of well control significantly reduce the inter-well flight time in various regions of the reservoir, resulting in a substantial improvement in reservoir connectivity. However, due to differences in permeability, the connectivity in the upper-left region remains lower than that in the lower-right region. Meanwhile, as the number of wells increases from 4 to 9 (Fig. 6(c) and (d)), the inter-well flight time decreases from 3964 to 2311 $s^{0.5}$, indicating further improvement in reservoir connectivity.

3.4.5. Development stage consideration

During the late stages of water flooding development, the overall fluid distribution in the reservoir undergoes significant changes compared to the early stages. Heterogeneity causes the gradual formation of dominant flow channels in high-permeability areas, resulting in ineffective water injection circulation. Additionally, fluid mobility in different parts of the reservoir varies with changes in relative permeability and differences in oil and water saturation. Taking the mechanism model of water flooding development for 0.5, 1, 2, and 4 years as examples, the oil saturation distribution is shown in Fig. 7. The results indicate that as water flooding progresses, oil displacement efficiency in high-permeability reservoirs steadily improves. Simultaneously, the

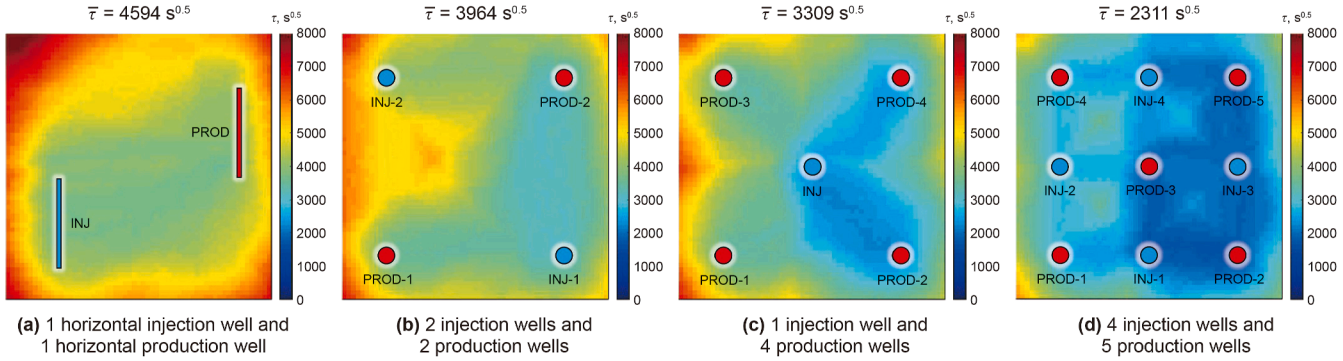

Fig. 6. Dynamic connectivity of reservoir with different well types and well patterns.

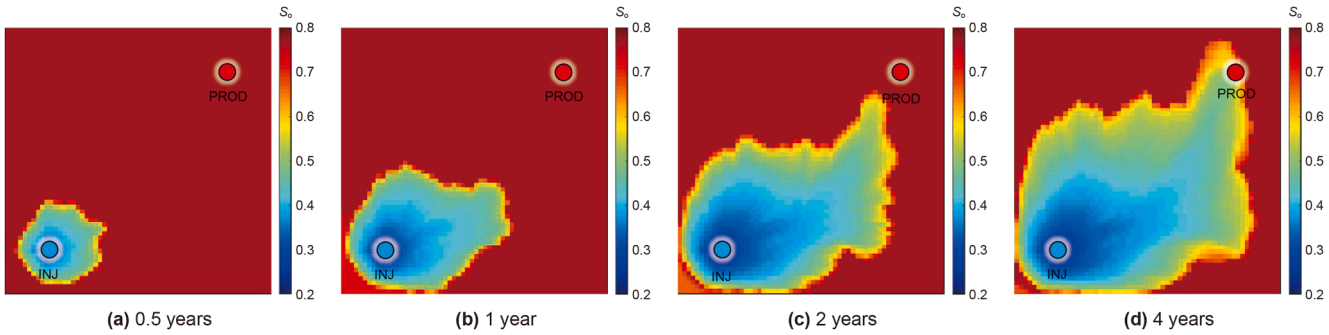

Fig. 7. Oil saturation distribution in different development stages.

connectivity of dominant flow channels in the reservoir improves due to the increased interface propagation speed. As development continues, the average inter-well flight time of the reservoir decreases from 5774 to 4085 $s^{0.5}$ (Fig. 8), reflecting the process in which higher-mobility water gradually displaces the oil, and a corresponding improvement in the overall connectivity of the reservoir.

4. Remaining oil potential evaluation method

4.1. Calculation of evaluation parameters

Due to variations in structural characteristics, reservoir properties, and fluid properties across different types of reservoirs, it is not feasible to directly measure the size of the remaining oil potential using parameters such as flight time or oil volume. Therefore, this study proposes an evaluation method based on relative values, utilizing the dynamic connectivity coefficient (*DC*) and remaining oil abundance coefficient (*ROA*), to enhance the development and evaluation of various types of reservoirs.

$$DC_i = \begin{cases} \dfrac{\tau_p - \tau_i}{\tau_p} & \tau_i < \tau_p \\ 0 & \tau_i \geq \tau_p \end{cases} \tag{12}$$

$$ROA_i = \begin{cases} \dfrac{\varphi_i S_{oi}}{\varphi_e S_{oe}} & \varphi_i S_{oi} < \varphi_e S_{oe} \\ 1 & \varphi_i S_{oi} \geq \varphi_e S_{oe} \end{cases} \tag{13}$$

where *DC* is dynamic connectivity coefficient; *ROA* is the remaining oil abundance coefficient; τ_i is the inter-well flight time at *i*-th grid; τ_p is the value of the *p*-th percentile inter-well flight time for the reservoir, different values can be selected for various types of reservoirs; S_{oi} is the oil saturation at *i*-th grid, dimensionless; S_{oe} is the initial average oil saturation of the reservoir, dimensionless; φ_i is the porosity at *i*-th grid; φ_e is the initial average porosity of the reservoir.

The *ROA* and *DC* are dimensionless coefficients designed to quantify variations in dynamic connectivity and remaining oil abundance in specific grid regions relative to the entire reservoir.

4.1.1. Remaining oil abundance coefficient (ROA)

The *ROA* is calculated as the ratio of the remaining oil in a specific grid to the average initial oil reserves of the reservoir. It is widely utilized as an index for analyzing remaining oil potential. It quantifies the degree of remaining oil utilization across different reservoir regions, with values ranging from 0 to 1. Higher *ROA* values reflect lower reservoir utilization in a specific region and indicate a greater abundance of remaining oil. In practice, ROA_i values may exceed 1 in high-porosity grids, especially during the early stages of production. To ensure consistency and comparability across regions, ROA_i is capped at 1 in this study. Specifically, when the product of porosity and oil saturation ($\varphi_i S_{oi}$) exceeds the average value ($\varphi_e S_{oe}$), ROA_i is limited to 1. As production progresses and local oil saturation decreases, ROA_i values in these grids naturally decline. This capping mechanism effectively prevents grids with abnormally high porosity from disproportionately influencing the evaluation results, thereby enhancing the stability and reliability of the proposed method.

4.1.2. Dynamic connectivity coefficient (DC)

The *DC* is calculated as the ratio of the inter-well flight time in a specific grid to the *p*-th percentile inter-well flight time of the entire reservoir. It represents the relative fluid flow capacity of a specific region compared to the overall reservoir. *DC* values range from 0 to 1. Higher values indicate stronger fluid flow capacity, identifying the region as a dominant flow zone. Conversely, lower

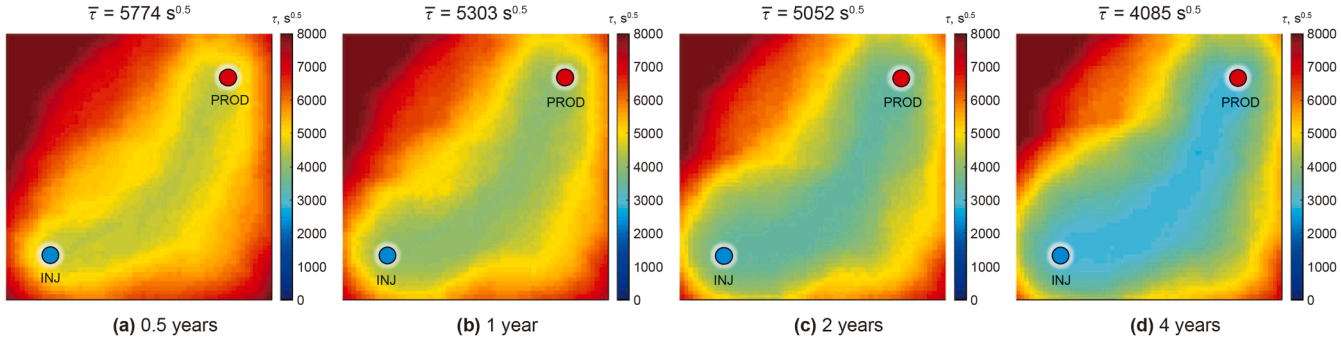

Fig. 8. Dynamic connectivity of reservoir in different development stages.

DC values suggest weaker flow capacity, often corresponding to unswept regions or areas with limited well control. The inter-well flight time is influenced by various factors, including reservoir type, structural characteristics, and fluid properties.

4.1.3. *p*-value selection and justification

Ideally, the *DC* values should be uniformly distributed between 0 and 1 to accurately reflect the overall heterogeneity of reservoir connectivity. However, due to the nature of flight time calculations, certain grid blocks, particularly those located in low-permeability regions, stagnant flow regions, or fault-shadowed areas, tend to exhibit abnormally high inter-well flight times. This skews the *DC* distribution and may overestimate connectivity in non-dominant flow regions, thereby reducing the contrast between areas with different flow capacities.

To minimize the influence of extreme values on evaluation results, this study introduces the *p*-th percentile inter-well flight time (τ_p) as a normalization reference, replacing the conventional arithmetic average. This approach preserves the overall connectivity trend while effectively reducing distortion caused by outliers, thereby enhancing the robustness of the *DC* distribution.

The selection of the *p*-value should be tailored to the connectivity characteristics of different reservoir types. In conventional reservoirs with relatively good connectivity and uniformly distributed preferential flow paths, only a small number of grid blocks present unusually high flight times (Fig. 9). In such cases, a higher *p*-value, typically in the range of 80–90, is appropriate filter out extreme values and to ensure a smoother and more representative *DC* distribution.

In contrast, low-permeability or highly faulted reservoirs often exhibit significant heterogeneity in connectivity. A considerable proportion of the grid blocks, sometimes exceeding 30%, may show high flight times due to low-permeability barriers or structural discontinuities (Fig. 10). Using a high *p*-value in such cases would include these extreme values in the normalization baseline τ_p. Consequently, the τ_i values of the majority of grid blocks within the main reservoir body become much smaller than τ_p, causing the resulting *DC* values to cluster near unity. This compresses the contrast between regions with varying connectivity, obscures dynamic connectivity differences within the main reservoir body, and ultimately distorts the evaluation outcomes. Therefore, a lower *p*-value, such as between 50 and 60, is thus more suitable for these reservoirs, as it better captures actual connectivity differences and improve the representativeness of the evaluation.

It is important to emphasize that the *p*-value must be selected flexibly according to the specific distribution of inter-well flight times in each reservoir. This adaptability ensures that the proposed method remains applicable and reliable across a wide range of reservoir conditions.

4.2. Bivariate mapping method

In the process of bivariate analysis, researchers need to address how to visually present the relationship and distribution between the two variables in a more intuitive manner. When variables are plotted individually, their relationships are often difficult to detect. Additionally, conventional direct classification often oversimplifies the data, leading to a loss of original details and making subsequent detailed analysis more challenging. To overcome these limitations, this study employed bivariate mapping for more refined analysis.

Bivariate mapping is a visualization technique that uses color coding to simultaneously reveal the size, correlation, differences, and other characteristics of two variables within a spatial area. This method is widely used in geography (Lucà et al., 2011), environmental science (Tehrany et al., 2014), public health (Khan and Mohanty, 2018), and other related disciplines. In this study, MATLAB was utilized to generate a 2D color map for the bivariate mapping of the *DC* and *ROA* parameters. The specific process is shown in Fig. 11. The resulting colormap effectively enhances the visualization and correlation of two variables, offering a novel analytical approach for future studies on remaining oil potential.

4.3. Evaluation chart of remaining oil potential

After obtaining the bivariate 2D color map, different reservoirs can be classified and analyzed in greater detail. In this study, reservoirs are divided into four potential evaluation regions based on the relationship between *DC* and *ROA* (Fig. 12):

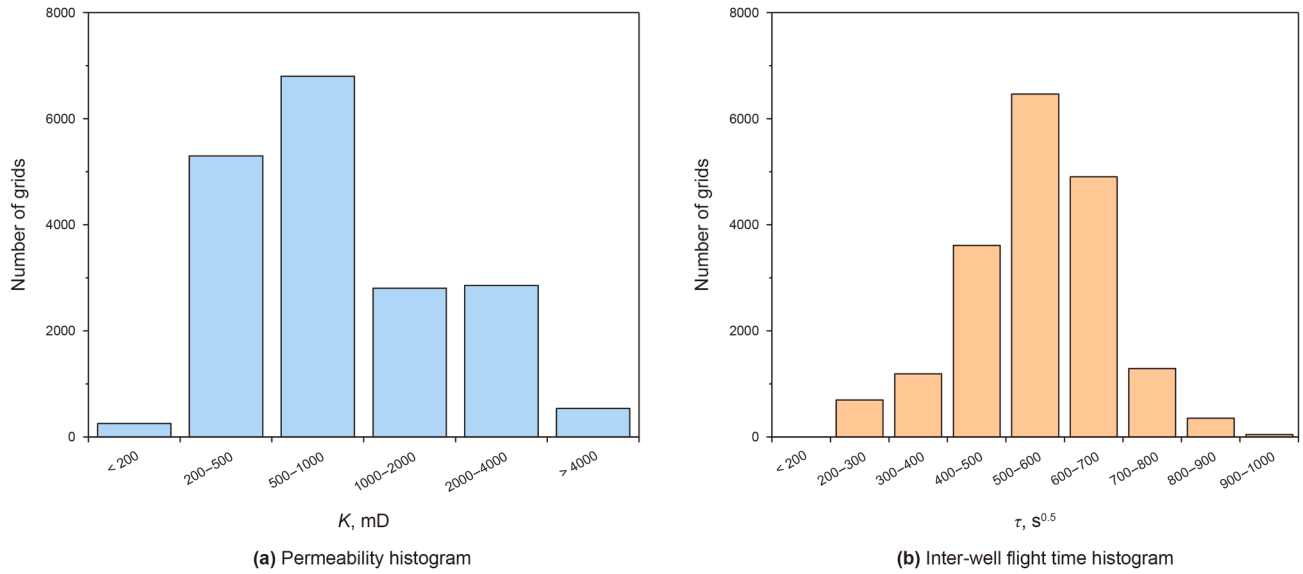

Fig. 9. Effect of permeability on inter-well flight time in a conventional reservoir.

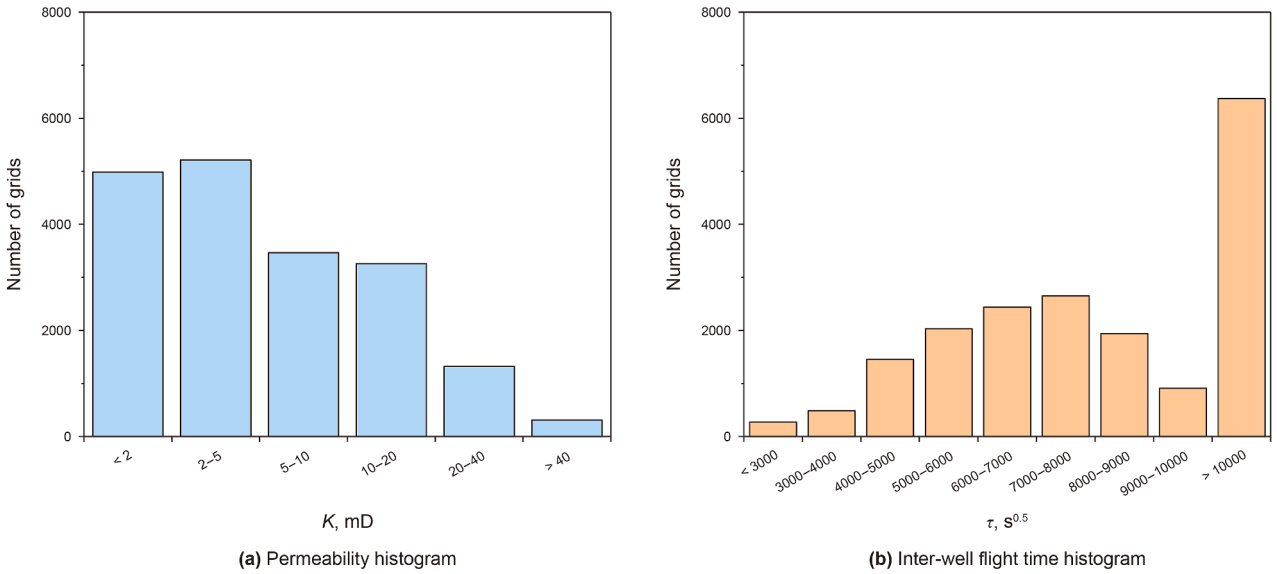

Fig. 10. Effect of permeability on inter-well flight time in a low-permeability reservoir.

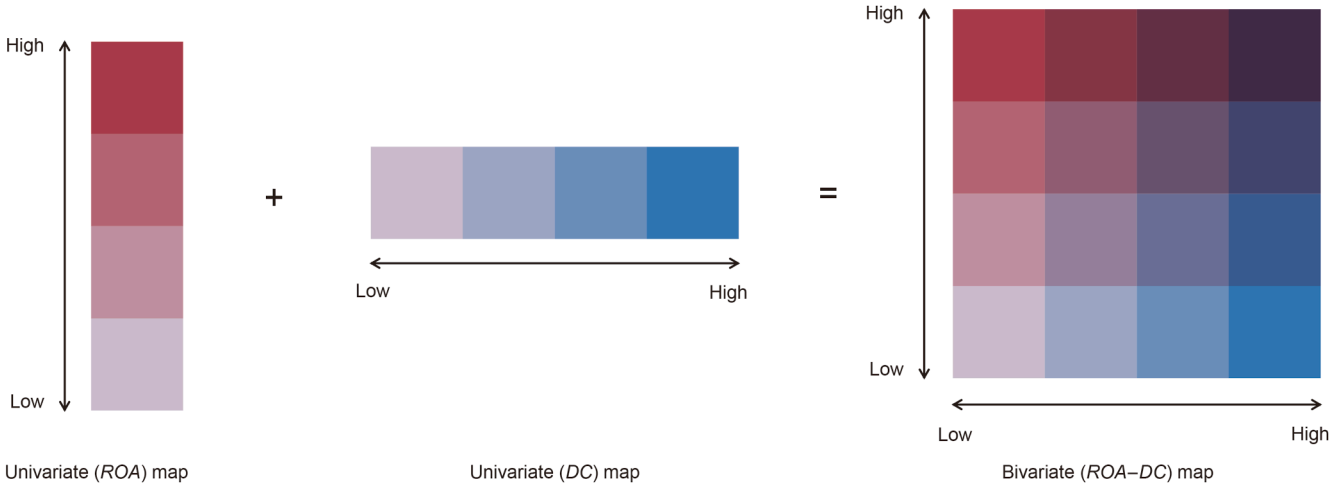

Fig. 11. Schematic of bivariable mapping.

4.3.1. Class I—uneconomic/awaiting measure region

The *DC* and *ROA* in this region are relatively low, typically indicating the presence of low-permeability zones at the edge of the reservoir. These regions exhibit poor utilization and low development potential. It typically requires an economic evaluation of development benefits, followed by measures such as acidification and fracturing to enhance development effectiveness.

4.3.2. Class II—low-efficiency waterflooding region

The *DC* in this region is relatively high, while the *ROA* is low. This typically occurs in preferential flow channels between wells, where the reservoir has been subjected to ineffective flushing over an extended period of time. These areas exhibit high fluid mobility but low development potential. Furthermore, this type of region often hinders the utilization of other low-connectivity zones. Therefore, it is necessary to optimize injection strategy in this area, reduce ineffective water injection circulation, and enhance the overall sweep efficiency and utilization rate of the reservoir.

4.3.3. Class III—major potential region

The *DC* in this region is relatively low, while the *ROA* is high, indicating an incomplete well pattern and a lower degree of well control in the region. These areas have high development potential and function as key adjustment zones in the later stages of reservoir development. Various measures, including injection–-production strategy improvements, infill wells, and horizontal well water control, can be implemented to enhance reservoir connectivity and improve the oil recovery rate of the entire reservoir.

4.3.4. Class IV—primary production region

Both *DC* and *ROA* are relatively high in this region, indicating that the reservoir is highly productive under the current well pattern and is the main contributor to oil production.

The boundaries for regional divisions are flexible due to the diversity of reservoir types and variations across different development stages. For *ROA*, the division boundaries are primarily determined by the reservoir's development stage. During the early development stage, when the overall *ROA* is relatively high, the

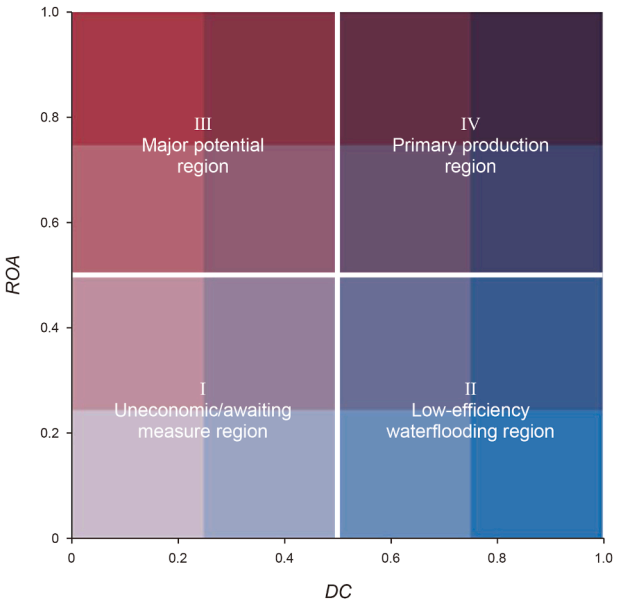

Fig. 12. Evaluation chart of remaining oil potential.

boundary is recommended within the range of 0.5–0.7. In contrast, during the later development stage, as *ROA* values decrease under high water-cut conditions, the boundary is advised to be adjusted to a range of 0.3–0.5.

For *DC*, the division boundaries are mainly influenced by type of reservoirs. In conventional medium-to-high permeability reservoirs with good connectivity, the *DC* boundary is recommended within the range of 0.5–0.7. However, in reservoirs characterized by extensive faulting or low permeability with poor connectivity, the boundary is advised to be adjusted to a range of 0.3–0.5.

4.4. 3D EGG reservoir model

This case study utilizes the EGG reservoir model as the foundational data source. The EGG reservoir model is a 3D channelized benchmark consisting of 60 ×60 × 7 grid cells, containing 18,553 active grid blocks. The dataset is publicly accessible at https://data.4tu.nl/articles/dataset/The_Egg_Model_-_data_files/12707642. The model consists of high-permeability dominant flow channels and medium-permeability regions, with permeability values ranging from 81 to 7000 mD and an average of 1137 mD (Fig. 13).

The initial formation pressure is 30 MPa, the initial oil saturation is 0.8, and the oil's viscosity and density are 20 mPa·s and 0.85 g/cm^3, respectively. The reservoir includes 8 production wells and 4 injection wells. Each production well has a daily liquid production rate of 40 m^3/d, while each injection well has a water injection rate of 80 m^3/d. The time step is set to 30 d, with a total production period of 1500 d.

The quantitative variations of *DC* and *ROA* with production time were calculated using Eqs. (12) and (13), as shown in Figs. 14–17. Subsequently, the bivariate mapping technique was employed for color visualization, effectively demonstrating the reservoir potential evaluation process and classification results in the EGG model (Fig. 21).

After considering the compressibility of rocks and fluids, the oil production at different grids is expressed by Eq. (14). Based on the numerical simulation results, post-processing analysis enables the determination of the number of different reservoir grids and the contribution of each unit grid to production, as shown in Figs. 18 and 19.

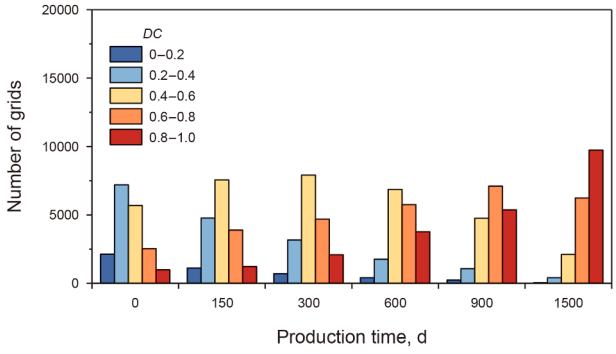

Fig. 14. *DC* histogram under different production times.

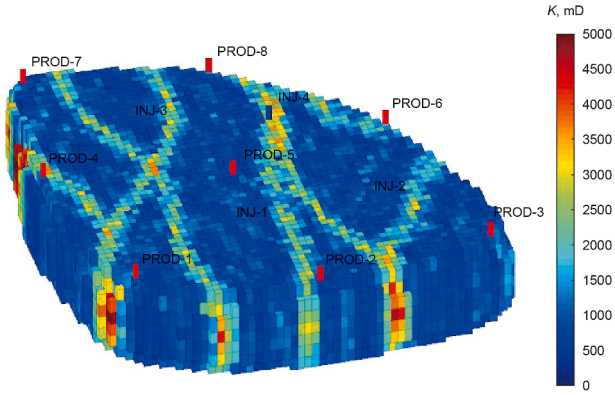

(a) Distribution

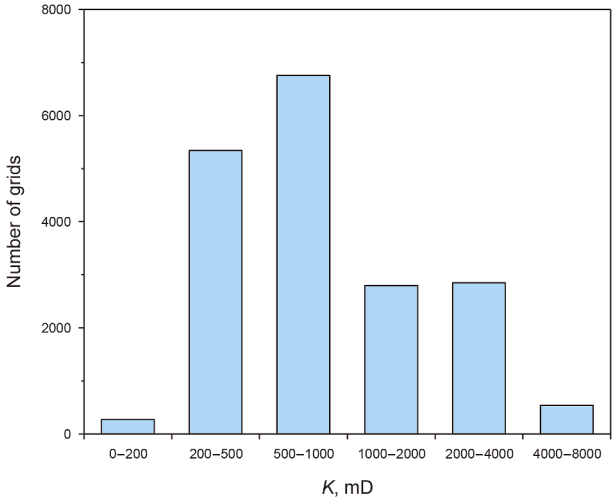

(b) Histogram

Fig. 13. Permeability distribution and histogram of EGG model.

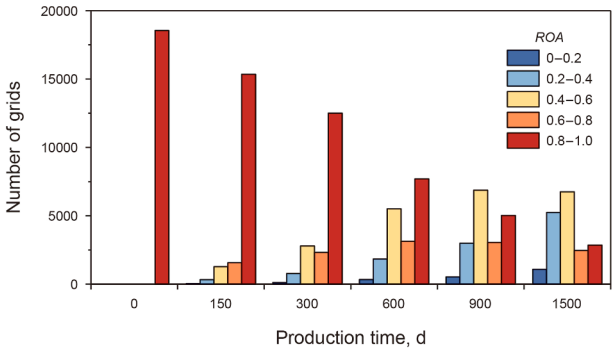

Fig. 15. *ROA* histogram under different production times.

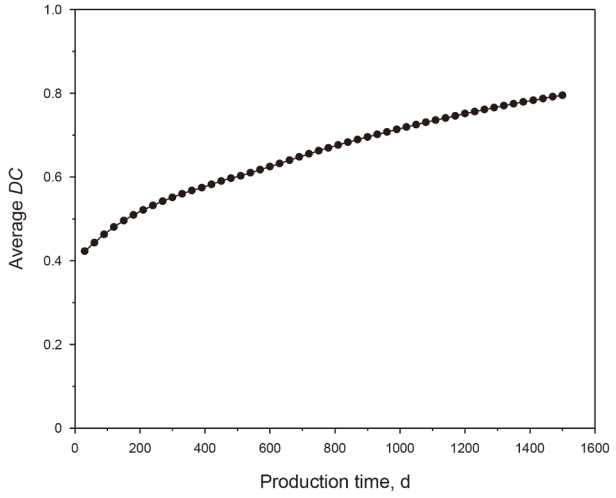

Fig. 16. Average *DC* under different production times.

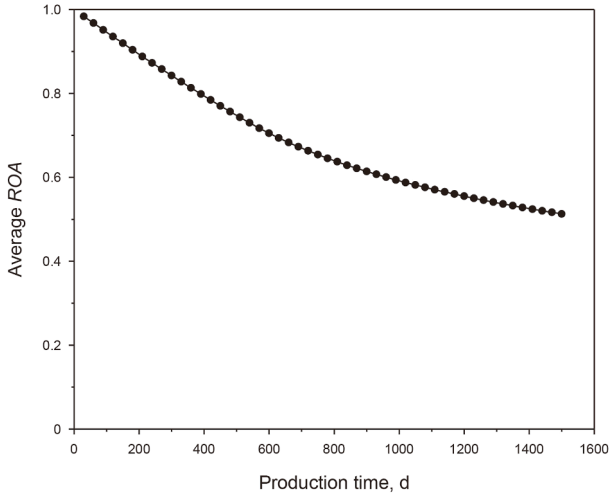

Fig. 17. Average *ROA* under different production times.

$$Q_o^k = \frac{1}{B_o}\Delta x_i \Delta y_i h_i \phi_i \left[S_{oi}^k (C_r + C_o)\left(p_i^{k+1} - p_i^k\right) + \left(S_{oi}^k - S_{oi}^{k+1}\right)\right] \quad (14)$$

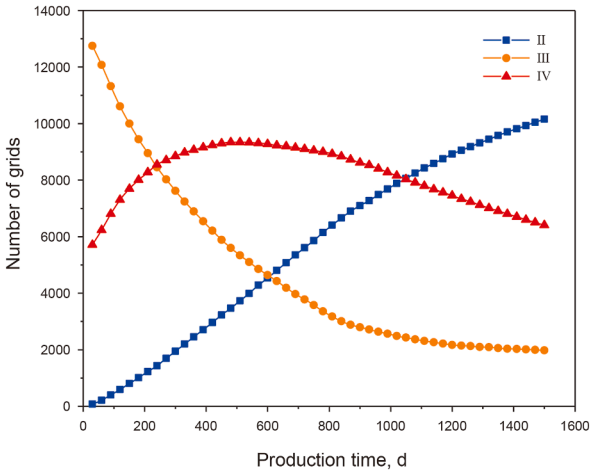

Fig. 18. The number of grids under different production times.

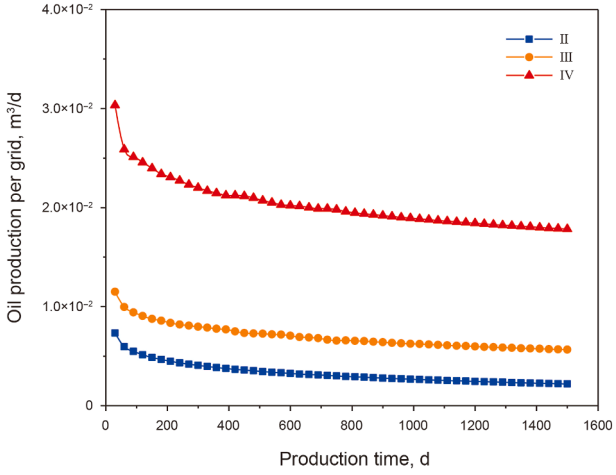

Fig. 19. Contribution of unit grid yield under different production times.

where Q_o^k is the oil production rate at time step k; B_o is the oil volume factor; Δx_i is the length of the i-th grid; Δy_i is the width of the i-th grid; h_i is the height of the i-th gird; S_{oi}^k is the oil saturation of the i-th grid at step k; C_r is the rock compressibility; C_o is the oil compressibility; p_i^k is the pressure of the i-th grid at step k.

Since the EGG reservoir model is a mechanistic model, it does not account for fault shadow zones or low permeability zones. Therefore, the proportion of Class I was extremely small in this mechanistic model, and thus specific analysis of these grids is not conducted. The results indicate the following:

(1) In the early production (0–300 d), the short production period and low cumulative injection volume resulted in a relatively uniform distribution of oil and water within the reservoir. At this stage, the overall dynamic connectivity of the reservoir was primarily influenced by the heterogeneous permeability distribution. As water injection progressed, the injected water preferentially flowed through the dominant high-permeability channels, gradually altering the connectivity within the reservoir. By the 300th day, the proportion of grids in low-to-moderate connectivity zones ($0 < DC < 0.4$) had

dropped from 50.3% to 20.9%, while grids with moderate-to-high connectivity ($0.4 < DC < 0.8$) increased from 44.3% to 67.9%. This marked the initial formation of dominant seepage pathways. Concurrently, the average *ROA* value decreased from 1.00 to 0.84, reflecting the gradual displacement of crude oil by injected water. Over time, this preferential flow enhanced the connectivity of Class III regions, transforming them into Class IV regions, which emerged as the primary contributors to production. During this period, the limited recovery degree kept the proportion of Class II regions relatively small and was largely confined to the near-well regions around the water injection wells.

(2) During the mid-term of production (300–900 d), as water flooding progressed, the difference in oil–water distribution became increasingly apparent compared to the initial state. The injected water primarily concentrated in the dominant high-permeability channel reservoirs, where the differences in oil and water mobility intensified the uneven fluid distribution. This process further enhanced the dynamic connectivity of high-permeability areas and strengthened the dominant seepage channels. Over this period, the proportion of grids in high-connectivity regions ($0.8 < DC < 1.0$) increased significantly from 11.2% to 29.0%, indicating substantial progress in the development of dominant flow paths. Meanwhile, the proportion of grids in high remaining oil regions ($0.8 < ROA < 1.0$) decreased markedly from 67.6% to 27.6%, suggesting that most of the reservoir had been effectively utilized. The average *ROA* value dropped significantly, from 0.84 to 0.62, reflecting the extensive displacement of crude oil by injected water. At this stage, as water flooding extended its reach, the Class III regions located at the edge of the river channels were progressively utilized and transformed into the main producing Class IV regions, becoming the main contributors to production.

(3) As the reservoir entered the late development stage, characterized by high water cut (900–1500 d), fluid mobility in the high-permeability zones increased further, reinforcing dominant seepage channels. Concurrently, the flow direction of injection water between injection and production wells gradually stabilized. During this period, the proportion of grids in high-connectivity regions ($0.8 < DC < 1.0$) further increased from 29.0% to 52.5%, highlighting the continued strengthening and stabilization of dominant seepage channels, along with an increase in the proportion of ineffective water circulation. The average *ROA* value dropped, from 0.6141 to 0.5100, while the proportion of grids in unutilized regions ($0.8 < ROA < 1.0$) decreased from 27.1% to just 16.2%. At this stage, as the water saturation in the main producing region (Class IV) continued to increase, the grid proportion in this category decreased, with some areas transitioned into Class II regions. Simultaneously, due to the solidification of the flow field, the proportion of Class III region grid numbers gradually stabilized, predominantly in low well-control areas and low connectivity non-advantageous flow areas.

4.5. Comparison and advantages with traditional methods

As shown in Fig. 20, the traditional evaluation process for remaining oil potential and streamline comparison is demonstrated. Traditional methods for assessing remaining oil potential typically rely on static indicators. While they allow for quantitative comparisons, the metrics used are limited and mostly focus on the analysis of remaining oil saturation. On the other hand, the traditional streamline comparison method accounts for fluid flow characteristics, but it is based on a qualitative comparison of streamline patterns, which makes it difficult to define the differences across regions quantitatively.

To address these limitations, this study emphasizes improving the comprehensiveness and quantitative nature of relative comparisons in the potential evaluation process. By comparing with Fig. 21, the proposed method shows significant improvements in the following areas:

1) More comprehensive comparison indicators: The method considers both dynamic and static regions, overcoming the limitations of traditional methods that rely solely on remaining oil saturation assessments, and compensating for the lack of fluid mobility analysis.
2) More quantitative evaluation approach: By constructing a quantitative evaluation chart, the method builds upon relative comparisons and incorporates fluid mobility analysis. This addresses the limitation of traditional streamline analysis, which

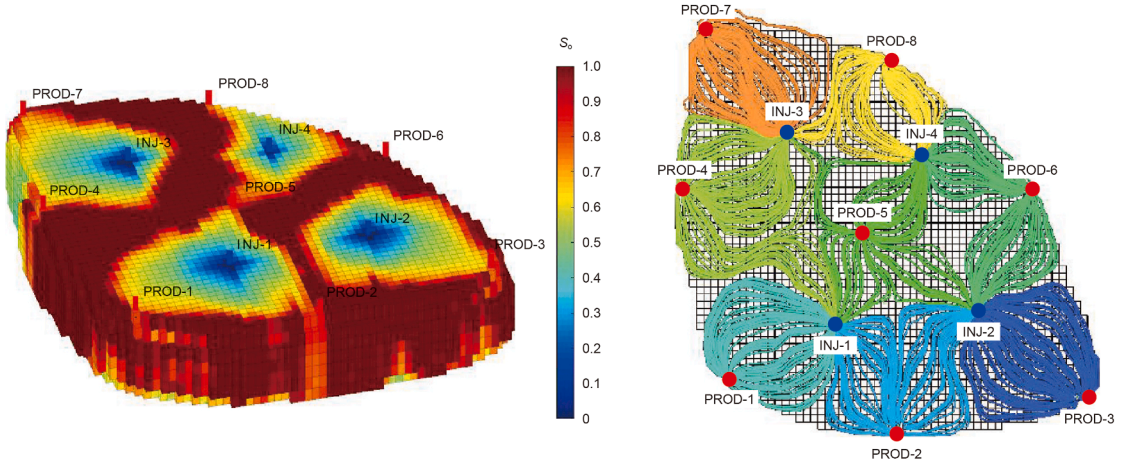

(a) Comparison of oil saturation

(b) Comparison of streamlines

Fig. 20. Traditional potential evaluation method.

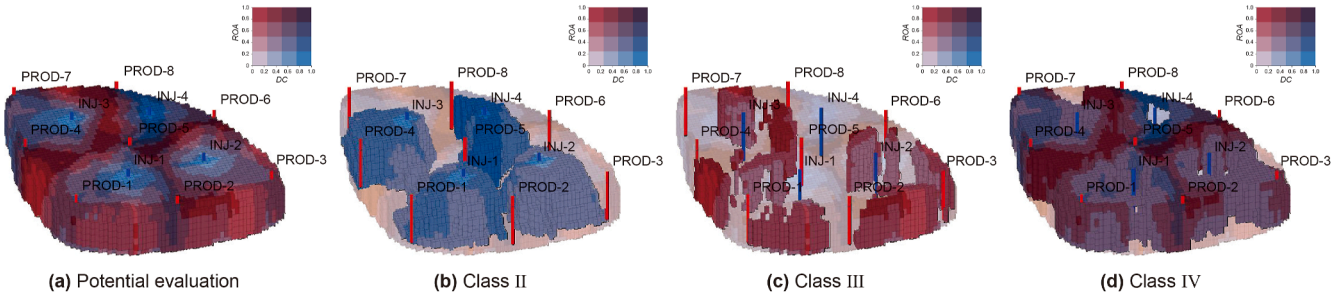

Fig. 21. Potential evaluation method in this paper.

only offers qualitative comparisons, thereby enhancing the operability of potential evaluations and making the potential differences across regions clearer and more comparable.

3) More intuitive comparison process: By employing bivariate mapping, the method displays two dimensions of information on a single image, significantly improving the visual clarity of the analysis.
4) More defined follow-up measures: Targeted development measures and potential directions have been formulated for different regions, enhancing the guidance and practicality of the evaluation.

These advantages demonstrate that the proposed method offers greater applicability and value in the process of reservoir potential evaluation, particularly in dynamic assessments of complex reservoirs and development decision-making.

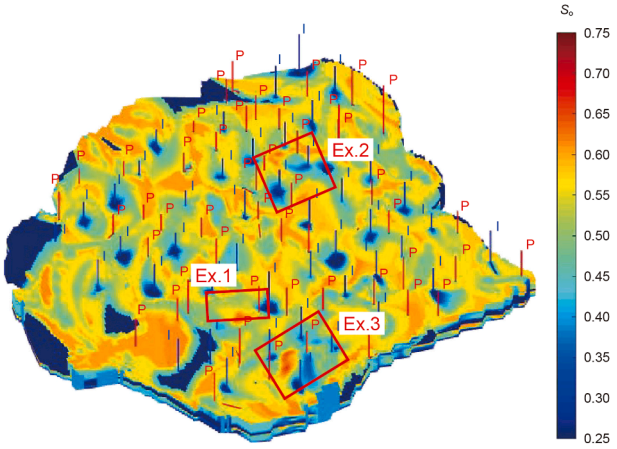

Fig. 23. Distribution of remaining oil in Nm I-3 Formation, M Oilfield.

5. Application in the M reservoir

The Nm I-3 Formation of the M Oilfield in the Bohai Sea is an unconsolidated sandstone reservoir with high porosity (33%) and high permeability (3374 mD) characteristics (Fig. 22). This block currently has over a hundred producing wells with a water cut exceeding 96.8% and a recovery factor reaching 36.7%. It has entered the high water-cut stage of development, with the distribution of oil saturation as shown in Fig. 23.

Given the long development history and frequent adjustments of the reservoir, tapping the remaining oil presents significant challenges. The primary issue lies in the most effective methods for identifying the remaining oil-enriched regions to stabilize oil production. The proposed method was applied to the target block to evaluate the remaining oil potential and guide subsequent exploitation efforts.

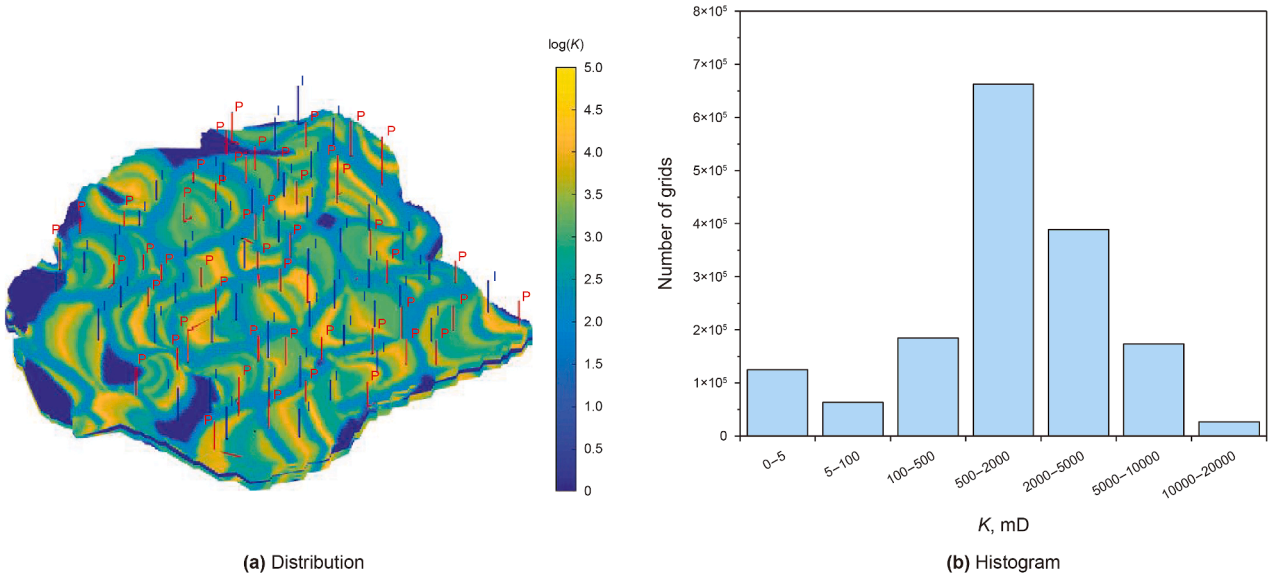

Fig. 22. Permeability distribution and histogram of EGG model.

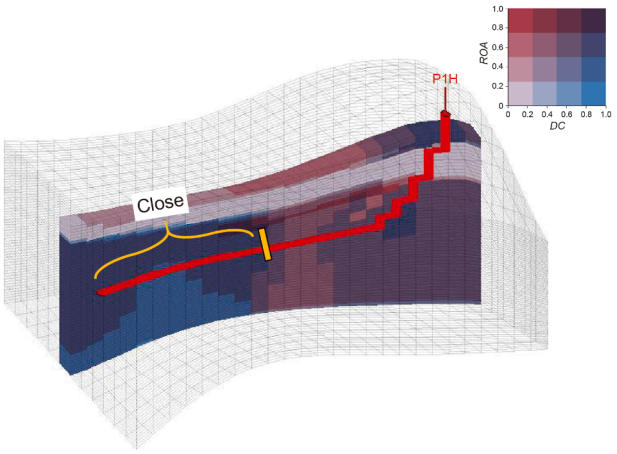

Fig. 24. Potential evaluation of P1H well cross-section.

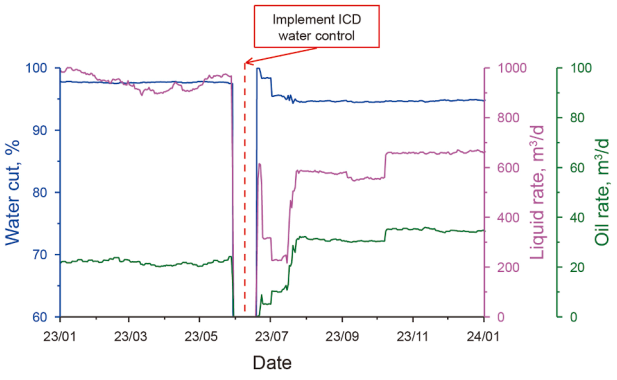

Fig. 25. Production curve of P1H well.

The suitability and application of the proposed method are demonstrated through three examples of remaining oil recovery.

5.1. Example 1: water control for horizontal well

The calculation results for the P1H cross-section (Fig. 24) indicate that the *ROA* is relatively high in the near root zone of the horizontal well (Class III), reflecting notable oil enrichment. However, the elevated *DC* in the toe segment (Class II) resulted in inefficient water circulation, significantly impairing connectivity in the root zone.

To address the poor dynamic connectivity along the horizontal wellbore, which led to accumulation of remaining oil, a water control strategy was implemented. This involved sealing the perforation section in the toe segment to improve the dynamic connectivity of the main potential region (Class III) in the proximal root region.

Following measure implementation of this measure, the production dynamics (Fig. 25) show that the water cut of the P1H well was reduced from 97.7% to 94.6%, the liquid rate decreased from 975 to 659 m^3/d, and the oil rate increased by 15 m^3/d.

5.2. Example 2: injection–production system adjustment in well group

The calculation results from the P2H well group (Fig. 26) indicate that, because of reservoir heterogeneity and the dominant water flow channels, the *DC* varied greatly within the internal well group. In the I4→P2H direction, the *ROA* was low (0–0.3), while the *DC* was high (0.7–1.0). Conversely, in the direction of I1→P2H, I2→P2H, and I3→P3H directions, the *DC* was relatively weak (0.3–0.7), while the *ROA* was relatively high (0.3–0.7). To enhance the production, the injection rate in weakly connected zone (I1→P2H, I2→P2H, I3→P3H) was increased.

Following the implementation of this measure, the production dynamics (Fig. 27) show a reduction in the water cut of the P2H well from 95.7% to 94.2%, and an increase in the oil rate from 25 to 32 m^3/d, reflecting a 33% increase.

5.3. Example 3: infill horizontal well

The calculation results (Fig. 28) for the P4H well group indicate that the dynamic connectivity within the group was similar to the P2H well group, exhibiting uneven utilization. However, unlike P2H well group, the I8→P4H direction was the primary injection path, while the *DC* in the I5→P4H, I6→P4H, and I7→P4H directions was lower (< 0.3). The greater variability in dynamic connectivity within the well group lead to injection-production imbalances that could not be resolved through injection strategy adjustments. To address this issue, a new horizontal well was infilled in the poorly controlled area of the well group.

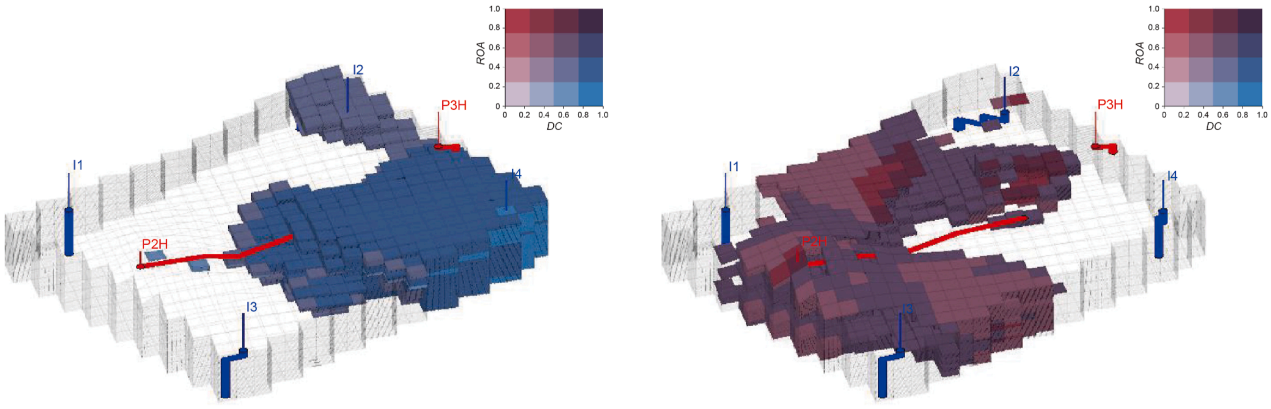

Fig. 26. Potential evaluation of P2H well.

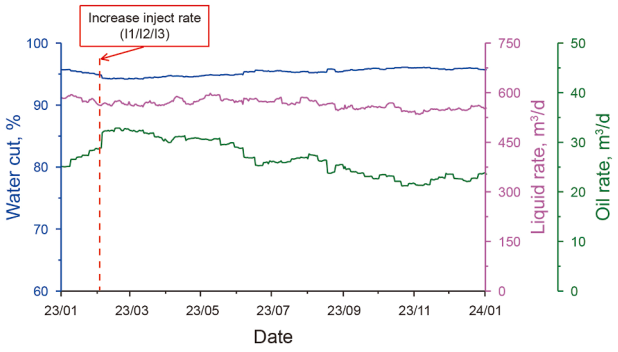

Fig. 27. Production curve of P2H well.

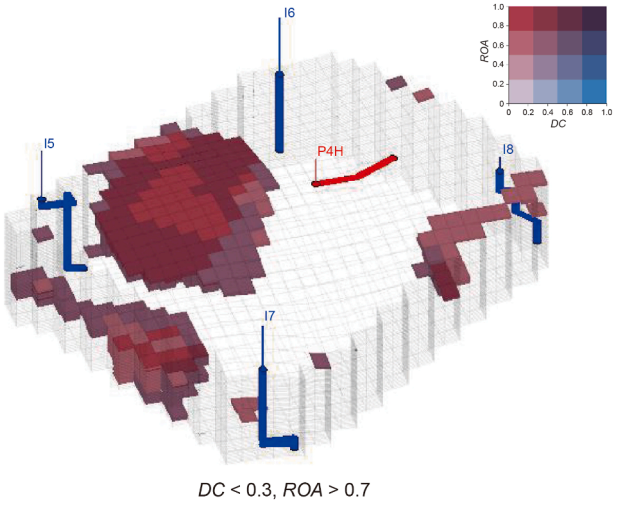

DC < 0.3, *ROA* > 0.7

Fig. 28. Potential evaluation of P4H well.

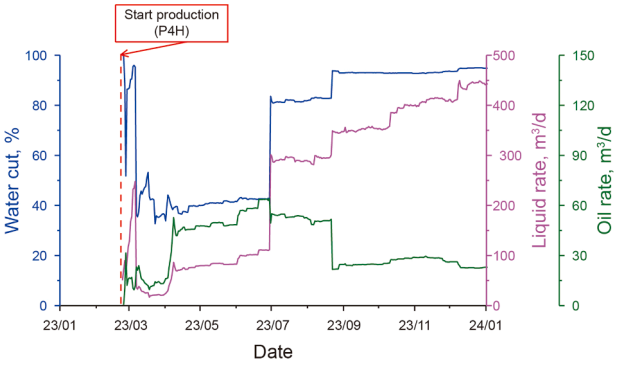

Fig. 29. Production curve of P4H well.

After the P4H well was put into operation, the production dynamics (Fig. 29) show that its initial oil rate reached 60 m^3/d, and after the water cut was stabilized, the oil rate was nearly 30 m^3/d. This result provided valuable insights and validated the implementing small well-spacing infill drilling in this block.

6. Conclusions

(1) A novel method for evaluating reservoir dynamic connectivity is proposed, leveraging the Eikonal equation's capability to accurately describe the pressure wavefront. This method effectively characterizes the dynamic connectivity of reservoirs with varying properties, well patterns, and development stages. It is especially suitable for analyzing the connectivity of large reservoirs with multiple wells.

(2) Based on the bivariate mapping approach, a novel full-life remaining oil potential evaluation method is developed, incorporating the dynamic connectivity coefficient (*DC*) and the remaining oil abundance coefficient (*ROA*). By using color encoding techniques, this methodology provides a visually intuitive way to analyze and assess reservoir potential across various regions under bivariate conditions. It significantly enhances the visualization of both dynamic and static reservoir characteristics and their interrelationships. Consequently, it offers clear insights into the development status, remaining oil potential, and optimal strategies for reservoirs of different classifications.

(3) The method was applied in the M oilfield, yielding promising results in three distinct scenarios aimed at enhancing recovery: horizontal well water control, injection–production system optimization, and infill horizontal well deployment. These successful outcomes demonstrate the method's suitability for complex, large-scale reservoirs. Additionally, the insights gained from these applications offer valuable guidance for implementing strategies in other oil and gas fields.

(4) Furthermore, the approach introduced in this study is fully integrated with entirely on established numerical simulation network data structures. Its seamless integration with existing numerical simulation models eliminates the need for complex data conversions and redundant computations.

CRediT authorship contribution statement

Jun-Da Wu: Writing – review & editing, Writing – original draft, Methodology, Investigation, Conceptualization. **Tao Chang:** Data curation, Conceptualization. **Yi-Fan He:** Supervision, Software, Resources. **Quan-Lin Wang:** Visualization, Validation. **Di Wang:** Supervision, Software, Project administration.

Conflict of interest

The paper has not been published before and is not under consideration for publication anywhere else; its publication has been approved by all co-authors, as well as by the responsible authorities-tacitly or explicitly-at the institute where the work has been carried out.

The authors declare no competing financial interests or personal relationships with other people or organizations.

Acknowledgment

This research was funded by comprehensive scientific research project of China National Offshore Oil Corporation (KJZH-2024-2204).

References

Alpak, F.O., Barton, M.D., Caers, J., 2010. A flow-based pattern recognition algorithm for rapid quantification of geologic uncertainty. Comput. Geosci. 14, 603–621. https://doi.org/10.1007/s10596-009-9175-5.

Augustine, C., Johnston, H., Young, D.L., et al., 2021. Evaluation of energy storage potential of unconventional shale reservoirs using numerical simulation of cyclic gas injection. J. Energy Resour. Technol. 143 (11), 112004. https://doi.org/10.1115/1.4049736.

Batycky, R.P., Thiele, M.R., 2016. Technology update: Mature flood surveillance using streamlines. J. Petrol. Technol. 68 (5), 22–25. https://doi.org/10.2118/0516-0022-JPT.
Chen, H., Park, J., Datta-Gupta, A., et al., 2020. Improving polymerflood performance via streamline-based rate optimization: Mangala Field, India. In: SPE Improved Oil Recovery Conference. https://doi.org/10.2118/200388-MS.
Cheraghi, Y., Kord, S., Mashayekhizadeh, V., 2021. Application of machine learning techniques for selecting the most suitable enhanced oil recovery method; challenges and opportunities. J. Petrol. Sci. Eng. 205, 108761. https://doi.org/10.1016/j.petrol.2021.108761.
Dam, M.H., Trieu, N.T., Tham, N.T., et al., 2023. Sequence stratigraphy and petrographic characteristics of Oligocene sediments in the West trough of the Cuu Long Basin, Vietnam. Mar. Petrol. Geol. 155, 106395. https://doi.org/10.1016/j.marpetgeo.2023.106395.
Datta-Gupta, A., King, M.J., 2007. Streamline Simulation: Theory and Practice, Vol. 11. Society of Petroleum Engineers, Houston, TX, USA.
Datta-Gupta, A., Xie, J., Gupta, N., et al., 2011. Radius of investigation and its generalization to unconventional reservoirs. J. Petrol. Technol. 63 (7), 52–55. https://doi.org/10.2118/0711-0052-JPT.
Hoffman, B.T., Reichhardt, D., 2020. Recovery mechanisms for cyclic (huff-n-puff) gas injection in unconventional reservoirs: A quantitative evaluation using numerical simulation. Energies 13 (18), 4944. https://doi.org/10.3390/en13184944.
Khan, J., Mohanty, S.K., 2018. Spatial heterogeneity and correlates of child malnutrition in districts of India. BMC Public Health 18 (1), 1027. https://doi.org/10.1186/s12889-018-5873-z.
Liu, R., Sun, Y., Yao, X., et al., 2022. Dynamic evaluation of flow unit based on reservoir evolution: A case study of Neogene Guantao Ng3 Formation in M Area, Gudao, Bohai Bay Basin. Geofluids 2022, 6249369. https://doi.org/10.1155/2022/6249369.
Lopez Jimenez, B.A., Aguilera, R., 2015. Flow units in shale condensate reservoirs. SPE Reservoir Eval. Eng. 19 (3), 450–465. https://doi.org/10.2118/178619-PA.
Lu, L., Sun, Y., Chang, C., et al., 2022. Fault reactivation in No. 4 structural zone and its control on oil and gas accumulation in Nanpu sag, Bohai Bay Basin, China. Petrol. Explor. Dev. 49 (4), 824–836. https://doi.org/10.1016/S1876-3804(22)60313-6.
Lu, Y., Liu, K., Xu, S., et al., 2020. Identifying flow units by FA-assisted SSOM—An example from the Eocene basin-floor-fan turbidite reservoirs in the Daluhu Oilfield, Dongying Depression, Bohai Bay Basin, China. J. Petrol. Sci. Eng. 186, 106695. https://doi.org/10.1016/j.petrol.2019.106695.
Lucà, F., Conforti, M., Robustelli, G., 2011. Comparison of GIS-based gullying susceptibility mapping using bivariate and multivariate statistics: Northern Calabria, South Italy. Geomorphology 134 (3–4), 297–308. https://doi.org/10.1016/j.geomorph.2011.07.006.
Mahdaviara, M., Sharifi, M., Ahmadi, M., 2022. Toward evaluation and screening of the enhanced oil recovery scenarios for low permeability reservoirs using statistical and machine learning techniques. Fuel 325, 124795. https://doi.org/10.1016/j.fuel.2022.124795.
Ramos, G.A., Akanji, L., 2017. Data analysis and neuro-fuzzy technique for EOR screening: Application in Angolan oilfields. Energies 10 (7), 837. https://doi.org/10.3390/en10070837.
Sethian, J.A., Popovici, A.M., 1999. 3-D traveltime computation using the fast marching method. Geophysics 64 (2), 516–523. https://doi.org/10.1190/1.1444558.
Siena, M., Guadagnini, A., Rossa, E.D., et al., 2016. A novel enhanced-oil-recovery screening approach based on Bayesian clustering and principal-component analysis. SPE Reservoir Eval. Eng. 19 (3), 382–390. https://doi.org/10.2118/174315-PA.
Sikanyika, E.W., Wu, Z., Mbarouk, M.S., et al., 2022. Numerical simulation of the oil production performance of different well patterns with water injection. Energies 16 (1), 91. https://doi.org/10.3390/en16010091.
Tabatabaei, S.M., Attari, N., Panahi, S.A., et al., 2023. EOR screening using optimized artificial neural network by sparrow search algorithm. Geoenergy Sci. Eng. 229, 212023. https://doi.org/10.1016/j.geoen.2023.212023.
Tehrany, M.S., Lee, M.J., Pradhan, B., et al., 2014. Flood susceptibility mapping using integrated bivariate and multivariate statistical models. Environ. Earth Sci. 72, 4001–4015. https://doi.org/10.1007/s12665-014-3289-3.
Vasco, D.W., Keers, H., Karasaki, K., 2000. Estimation of reservoir properties using transient pressure data: An asymptotic approach. Water Resour. Res. 36 (12), 3447–3465. https://doi.org/10.1029/2000WR900179.
Wang, J., Fan, Z., Zhao, L., et al., 2020. Effects of oil viscosity on waterflooding: A case study of high water-cut sandstone oilfield in Kazakhstan. Open Geosci. 12 (1), 1736–1749. https://doi.org/10.1515/geo-2020-0218.
Zhang, N., Wei, M., Fan, J., et al., 2019. Development of a hybrid scoring system for EOR screening by combining conventional screening guidelines and random forest algorithm. Fuel 256, 115915. https://doi.org/10.1016/j.fuel.2019.115915.
Zhang, N., Cao, J., James, L., et al., 2021. High-order streamline simulation and macro-scale visualization experimental studies on waterflooding under given pressure boundaries. J. Pet. Sci. Eng. 203 (1), 108617. https://doi.org/10.1016/j.petrol.2021.108617.
Zhang, N., Wei, M., Bai, B., et al., 2022. Pattern recognition for steam flooding field applications based on hierarchical clustering and principal component analysis. ACS Omega 7 (22), 18804–18815. https://doi.org/10.1021/acsomega.2c01693.
Zhao, R., Zhao, T., Kong, Q., et al., 2020. Relationship between fractures, stress, strike-slip fault and reservoir productivity, China Shunbei oil field, Tarim Basin. Carbonates Evaporites 35 (3), 84. https://doi.org/10.1007/s13146-020-00612-6.
Zhu, C., Jiang, F., Zhang, P., et al., 2021. Identification of effective source rocks in different sedimentary environments and evaluation of hydrocarbon resources potential: A case study of Paleogene source rocks in the Dongpu Depression, Bohai Bay Basin. J. Petrol. Sci. Eng. 201, 108477. https://doi.org/10.1016/j.petrol.2021.108477.
Zubkov, M.Y., 2017. The reservoir potential of the Bazhenov Formation: Regional prediction. Russ. Geol. Geophys. 58 (3–4), 410–415. https://doi.org/10.1016/j.rgg.2016.09.016.